Condensed Matter Physics, 2025, Vol. 28, No. 3, 33702: 1–11
DOI: 10.5488/CMP.28.33702
http://www.icmp.lviv.ua/journal

CONDENSED MATTER PHYSICS

Beyond conventional half-metals: gapless states and spin gapless semiconducting behavior in X_2MnGa (X = Ti, Ir) Heusler compounds*

N. Bouteldja [1†], N. Hacini [2], I. Ouadha [3], H. Rached [3]

[1] Theoretical Physics and Materials Physics Laboratory, Hassiba Benbouali University, Chlef, Algeria
[2] Condensed Matter Sciences Laboratory, Oran 1 Ahmed Ben Bella University, Oran, Algeria
[3] Magnetic Materials Laboratory, Djillali Liabes University, Sidi Bel-Abbes, Algeria

Received May 19, 2025, in final form July 11, 2025

The search for high-performance spintronic materials motivates the exploration of Heusler alloys with unconventional electronic properties. Using density functional theory with Hubbard correction (DFT+U, $U = 4$ eV), we investigate X_2MnGa (X = Ti, Ir) alloys, which stabilize in the ferromagnetic $L2_1$-type structure with strong thermodynamic stability. Electronic structure calculations reveal contrasting behaviors: Ti_2MnGa transitions from a metallic $L2_1$-type phase to a spin gapless semiconductor (SGS) in the XA-type, while Ir_2MnGa exhibits gapless half-metallicity behavior in the $L2_1$-type but becomes half-metallic in the XA-type. The magnetic properties are governed by *spd* hybridization between Mn-3d and X-d/Ga-p states, which stabilizes ferromagnetism and tailors electronic states near the Fermi level. The Hubbard U correction proves essential for accurately describing the correlated Mn-3d electrons. These alloys combine structural stability with tunable electronic and magnetic properties, offering a promising platform for spin-polarized transport in next-generation spintronic devices.

Key words: *Heusler alloys, spintronics, DFT+U, spin gapless semiconductors, half-metals, magnetic materials*

1. Introduction

The accelerated development of spintronic systems, which exploit both the charge degree of freedom and quantum-mechanical spin of electrons, has necessitated the discovery and design of advanced functional materials with precisely tunable electronic structure and magnetic order parameters. Among the most promising candidates are Heusler alloys, a versatile class of intermetallic compounds that exhibit remarkable functionalities such as half-metallic ferromagnetism, 100% spin polarizability and high Curie temperatures, making them ideal for spin-based electronics [1, 2]. These materials have found applications in magnetic random-access memory (MRAM), spin-injection devices, high-density data storage technologies, giant, tunnel and colossal magnetoresistive (GMR, TMR, CMR) sensors [3–5].

Heusler alloys are broadly categorized into full-Heusler (X_2YZ) and half-Heusler (XYZ) structures, where X and Y are typically transition metals and Z is a main-group element. Their electronic structure can be precisely tuned by varying composition, leading to diverse transport behaviors [6], including half-metallic (HM), spin gapless semiconducting (SGS) and gapless half-metallic (GHM) states [7–10].

The exceptional magnetic properties of Heusler alloys stem from the strong *spd* hybridization between transition metal (Mn, Co, Fe, . . .) d-states and main-group (Ga, Al, Si, . . .) p-states, which governs their electronic and magnetic behavior. This hybridization leads to the formation of spin-polarized bands near the Fermi level, stabilizing ferromagnetic (FM) or ferrimagnetic (FiM) ordering. The nature of magnetic

*". . . I wouldn't stand by and see the rules broken — because right is right, and wrong is wrong, and a body ain't got no business doing wrong when he ain't ignorant and knows better." (Twain M., *The Adventures of Huckleberry Finn*, 1884).

†Corresponding author: n.bouteldja@univ-chlef.dz.

coupling in these alloys is highly sensitive to atomic arrangement, composition and interatomic distances, allowing for precise tuning of their magnetic moments and exchange interactions [11–13].

In full-Heusler alloys (X_2YZ), the magnetic moment is primarily localized on the transition metal (X, Y) sites, with Mn-based alloys often exhibiting high spin polarization due to their half-filled 3*d* orbitals [14]. Co-based Heusler alloys (Co_2MnSi, Co_2FeAl, ...) are classic half-metallic ferromagnets [15–17], where one spin channel is metallic while the other is semiconducting, enabling 100% spin-polarized currents. Ferrimagnetic Heusler alloys (Mn-based compounds) exhibit compensated magnetic moments [18–20], where antiparallel alignment of Mn spins results in a net zero magnetization, making them ideal for low-energy-loss spintronic devices.

Martensitic transformations in Mn-rich Heusler alloys (Ni-Mn-Ga, Ni-Mn-In, Ni-Mn-Sn, ...) enable remarkable multifunctional properties [21–23], including temperature or stress induced shape-memory effects (SME) and giant magnetocaloric effects (MCE), facilitating applications in magnetic shape-memory actuators and strain-mediated spintronics where magnetic anisotropy is controlled through lattice deformation. Beyond these conventional properties, recent discoveries have unveiled novel electronic states in Heusler alloys. SGS like Cr_2ZnSi [24] exhibit a direct touch between the valence and conduction bands at the Fermi level in one spin channel, enabling fully spin-polarized transport with minimal energy excitation, ideal for low-power spintronics. Similarly, Ti_2MnAl [25] shows bandgap closure in the spin-up channel, allowing near-zero-energy spin-polarized conduction for high-speed devices. Meanwhile, Mn_3Ga [26] exhibits characteristic gapless half-metallic behavior with 100% spin polarization, featuring a unique electronic structure where one spin channel shows gapless semiconducting properties while the other remains metallic. Theoretical studies suggest that this material possesses compensated ferrimagnetic ordering and may undergo martensitic transformations, similar to the related Mn-based Heusler alloys. These Heusler compounds, with their unique electronic structures and magnetotransport properties, are pivotal for advanced spintronics.

In this work, we employ state-of-the-art first-principles calculations incorporating Hubbard *U* corrections (DFT+*U*) to conduct a comprehensive and systematic investigation of the structural, electronic and magnetic properties of X_2MnGa (X = Ti, Ir) Heusler alloys. Our computational approach combines density functional theory with the generalized gradient approximation (GGA-PBE) for exchange-correlation effects, augmented by a Hubbard *U* correction of 4.0 eV applied to the strongly correlated 3*d*-5*d*-4*f* states in order to accurately capture their localized character and hybridization effects.

2. Calculation details

To account for strong electron correlations, first-principles calculations were performed using the full-potential linearized augmented plane-wave (FPLAPW) method as implemented in the WIEN2κ code [27, 28], within the framework of density functional theory (DFT) [29]. The exchange-correlation effects were treated using the GGA-PBE [30], with an additional Hubbard *U* correction (GGA+*U*, $U = 4.0$ eV) applied to the Mn-3*d* states to account for strong electron correlations [31]. This approach mitigates the self-interaction error in standard GGA for localized *d*-electrons. The muffin-tin radii (R_{MT}) were chosen to satisfy $R_{MT} \times K_{max} = 8.0$, ensuring a well-converged basis set, while Brillouin zone integration was carried out using a $10 \times 10 \times 10$ **k**-mesh (1000 **k**-points). The self-consistent calculations converged with an energy criterion of 10^{-5} Ry for electronic relaxation. The electronic configurations of the constituent elements were explicitly considered to accurately describe their valence states and hybridization effects in the system: Ti ($3d^2 4s^2$), Ir ($4f^{14} 5d^7 6s^2$), Mn ($3d^5 4s^2$) and Ga ($3d^{10} 4s^2 4p^1$).

3. Spin-dependent bandscapes

Figure 1 illustrates four distinct types of spin-dependent band structures, each enabling unique functionalities in spintronics: (a) GHM exhibit Dirac-like metallic spin-↑ states with linear dispersion, while spin-↓ remains semiconducting with zero bandgap, enabling high-speed spintronic devices [32, 33]; (b) SGS have gapless spin-↑ bands (zero DOS at E_F) while spin-↓ bands are gapped, enabling ultra-low-power spin transistors and quantum sensors [34]; (c) HM are 100% spin-polarized (↑=metallic,

↓=semiconducting), ideal for MRAM and spin injection [35, 36]; (d) magnetic metals (MM) conduct both spin-↑ and spin-↓ electrons with partial spin polarization, making them useful for spin valves and GMR sensors [37].

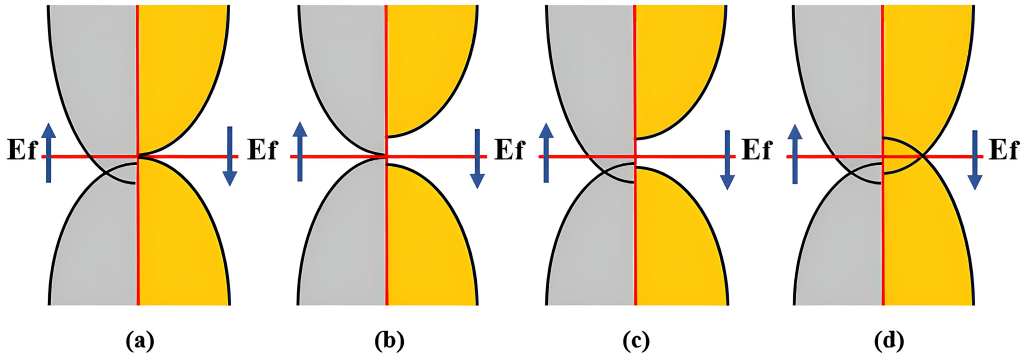

Figure 1. (Colour online) Spin-polarized band structures: (a) gapless half-metal, (b) spin gapless semiconductors, (c) half-metals, (d) magnetic metal.

4. Results and discussion

4.1. Structural properties

The crystal structures of the full Heusler alloy X_2MnGa (X = Ti, Ir) are shown in figure 2, displaying both: (a) the conventional $L2_1$-type structure (space group $Fm\bar{3}m$, No. 225), (b) the inverse Heusler XA-type structure (space group $F\bar{4}3m$), where both structures consist of four interpenetrating face-centered cubic (fcc) sublattices with distinct atomic arrangements: in the $L2_1$-type structure, the Ti/Ir atoms occupy the (0.25, 0.25, 0.25) and (0.75, 0.75, 0.75) Wyckoff positions, Mn occupies (0, 0, 0) and Ga is located at (0.5, 0.5, 0.5), while for the inverse XA-type structure, one Ti/Ir atom sits at (0, 0, 0), another at (0.25, 0.25, 0.25), Mn at (0.5, 0.5, 0.5) and Ga at (0.75, 0.75, 0.75), with muffin-tin radii (R_{MT}) typically chosen as Ti = 2.2, Ir = 2.5, Mn = 2.0 and Ga = 2.1 atomic units to ensure a proper overlap in the DFT calculations while minimizing computational artifacts.

To determine the stable ground-state configurations, we performed total energy versus volume (E–V) calculations for both the $L2_1$-type and XA-type structures, then fitted the data using the Birch–Murnaghan equation of state [38].

$$E(V) = E_0 + \frac{B}{B'(B'+1)}\left[V\left(\frac{V_0}{V}\right)^{\beta} - V_0\right] + \frac{B}{B'}(V-1). \tag{4.1}$$

Figure 3 compares the total energies of: (a) Ti_2MnGa, (b) Ir_2MnGa in $L2_1$-type ($Fm\bar{3}m$) and XA-type ($F\bar{4}3m$) configurations. Our calculations confirm that the $L2_1$-type structure is energetically favorable, exhibiting a lower total energy than the XA-type structure. This stabilization primarily originates from optimized chemical bonding and hybridization effects between the constituent elements. In the $L2_1$ structure, the Mn atoms occupy a high-symmetry position that maximizes favorable d–d orbital overlap with neighboring transition metals (Ti/Ir) while maintaining optimum charge transfer to Ga sp-states. This coordination geometry enhances covalent bonding and band filling efficiency compared to the XA-type structure, resulting in greater thermodynamic stability.

Table 1 presents the computed structural parameters of X_2MnGa (X = Ti, Ir). The lattice constants (a) were optimized through energy-volume calculations and the bulk modulus (B) along with its pressure derivative (B') were extracted from Birch–Murnaghan equation of state fitting. The corresponding equilibrium energy (E_0) at the minimum energy configuration is also reported.

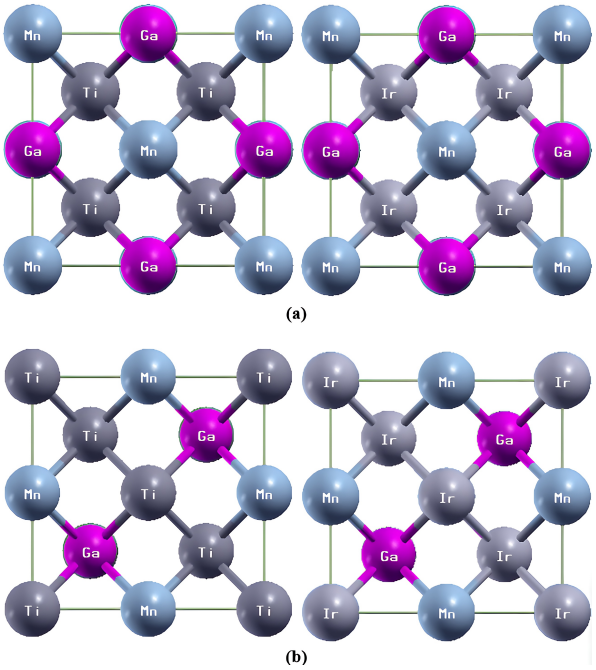

Figure 2. (Colour online) Crystal structures of Ti_2MnGa and Ir_2MnGa: (a) conventional $L2_1$-type structure (space group $Fm\bar{3}m$) and (b) inverse XA-type structure (space group $F\bar{4}3m$).

The calculated structural parameters reveal several key trends. The $L2_1$-type phase consistently exhibits smaller lattice parameters (a) compared to the XA-type structure for both compounds, indicating denser atomic packing. Bulk modulus (B) values are considerably higher in the $L2_1$-type phase (148.99 GPa for Ti_2MnGa compared with 236.17 GPa for Ir_2MnGa), demonstrating greater structural rigidity. The pressure derivative (B') values between 3.77–5.64 suggest normal elastic behavior for all configurations. The lower minimum energies (E_{min}) of the $L2_1$-type phase confirm its thermodynamic stability over the XA-type structure, with energy differences of 0.0228 Ry (Ti_2MnGa) and 0.1432 Ry (Ir_2MnGa), respectively. These results correlate with the stronger d–d hybridization in the $L2_1$ configuration observed in our electronic structure analysis.

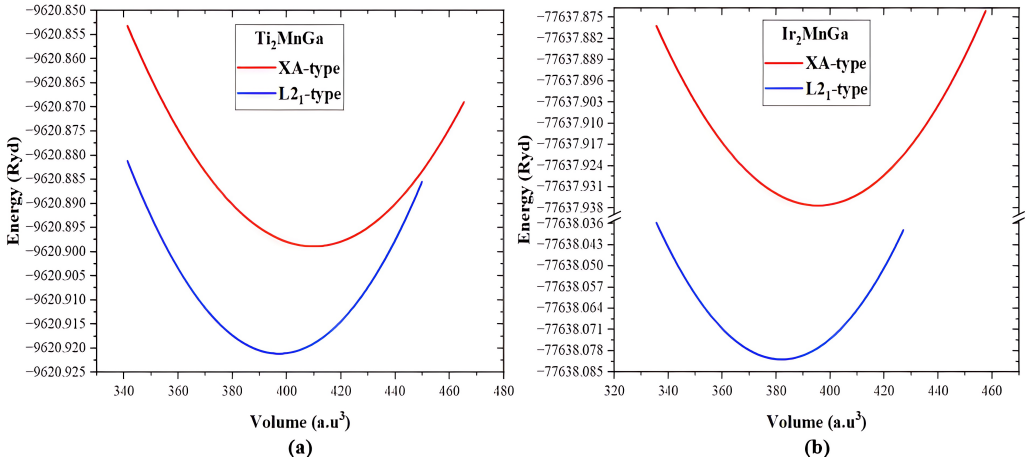

Figure 3. (Colour online) Energy versus volume curves for (a) Ti_2MnGa and (b) Ir_2MnGa in both $L2_1$-type and XA-type structures, calculated using PBE+U (U = 4 eV).

Table 1. Lattice parameters and properties of Ti_2MnGa and Ir_2MnGa compounds calculated via PBE+U.

Property	**$L2_1$ ($Fm\bar{3}m$)**		**XA ($F\bar{4}3m$)**	
	Ti_2MnGa	**Ir_2MnGa**	**Ti_2MnGa**	**Ir_2MnGa**
Lattice constant a (Å)	5.9138	5.8461	5.9815	5.9036
Bulk modulus B (GPa)	148.9958	236.1689	108.9095	199.1957
Pressure derivative B'	5.6251	5.1368	3.7698	4.6396
Minimum energy E_{min} (Ry)	−9620.921074	−77638.080872	−9620.898279	−77637.937667

4.2. Electronic properties

4.2.1. Band structure

The electronic band structures of X_2MnGa (X = Ti, Ir) Heusler alloys reveal fundamentally distinct spin-dependent behaviors, as shown in figures 4 and 5. These differences originate from their unique electronic configurations, which dramatically influence their spin-polarized transport properties.

Ti_2MnGa in the XA-type structure exhibits a characteristic spin gapless semiconductor behavior (confirmed by [39]). As visible in Figure 4b, the spin-↑ channel presents an indirect band gap of 0.528 eV between the Γ and L points, while the spin-↓ channel forms a zero-gap configuration, where the valence and conduction bands touch precisely at the Fermi level (E_F). This unique band alignment enables efficient spin-polarized transport, as charge carriers in the spin-↓ channel can be excited without overcoming an energy barrier, while the spin-↑ channel remains semiconducting. When transformed to the $L2_1$-type structure (figure 4a), this delicate SGS configuration is lost. Both spin channels cross E_F, resulting in a conventional ferromagnetic metallic state. The disappearance of the SGS behavior in the $L2_1$ phase can be attributed to the altered crystal field splitting and hybridization between the Ti-3d, Mn-3d, and Ga-4p orbitals, which modifies the band structure near E_F. This transition underscores the critical role of atomic ordering in determining the electronic properties.

Ir_2MnGa demonstrates markedly different electronic behavior compared to its Ti counterpart, as evidenced in figure 5a. The strong spin-orbit coupling (SOC) from iridium 5d electrons plays a decisive role in shaping its electronic structure. In the $L2_1$-type phase, the system exhibits a rare gapless half-metallic state, the spin-↑ channel shows metallic conductivity with bands crossing the Fermi level (E_F), while the spin-↓ channel forms a zero-gap configuration where the valence and conduction bands touch at E_F. This unique state arises from the interplay between SOC-induced band splitting and the specific symmetry of the $L2_1$ lattice, which preserves degeneracies at certain high-symmetry points. When transformed to the XA-type structure (figure 5b), Ir_2MnGa transitions to a standard half-metal (confirmed by [40]). The spin-↑ channel opens an indirect band gap of 0.212 eV between the Γ and X points, while the spin-↓ channel becomes metallic with band overlap at E_F. This change stems from the XA structure lower symmetry, which breaks degeneracies and enhances exchange splitting compared to the $L2_1$ phase. The result is a clear separation between valence and conduction bands in the minority spin channel while maintaining metallic conductivity in the majority spins.

These results demonstrate how electronic properties are intimately connected to both crystal structure and elemental composition. The Ti system shows particular phase sensitivity, while the Ir compound maintains robust spin polarization across structures. The comparative analysis reveals the complex interplay between spin-orbit coupling and crystal symmetry in these technologically important materials.

4.2.2. Density of states

Figure 6 illustrates the spin-dependent total and atomic density of states (DOS) for Ti_2MnGa and Ir_2MnGa in both $L2_1$-type and XA-type structural configurations.

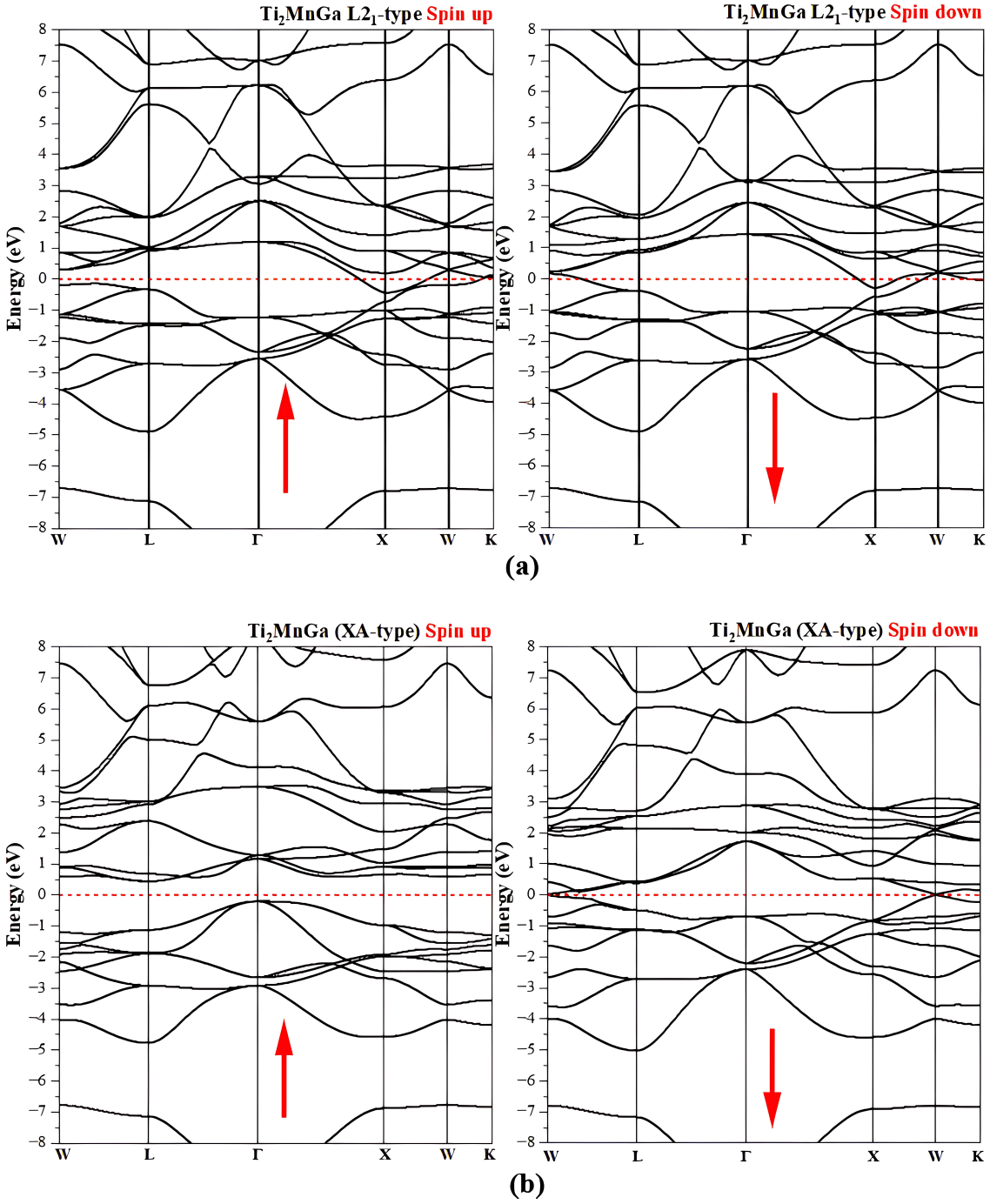

Figure 4. (Colour online) Spin-polarized band structure of Ti_2MnGa calculated using PBE+U (U = 4 eV) for both (a) $L2_1$-type and (b) XA-type structures.

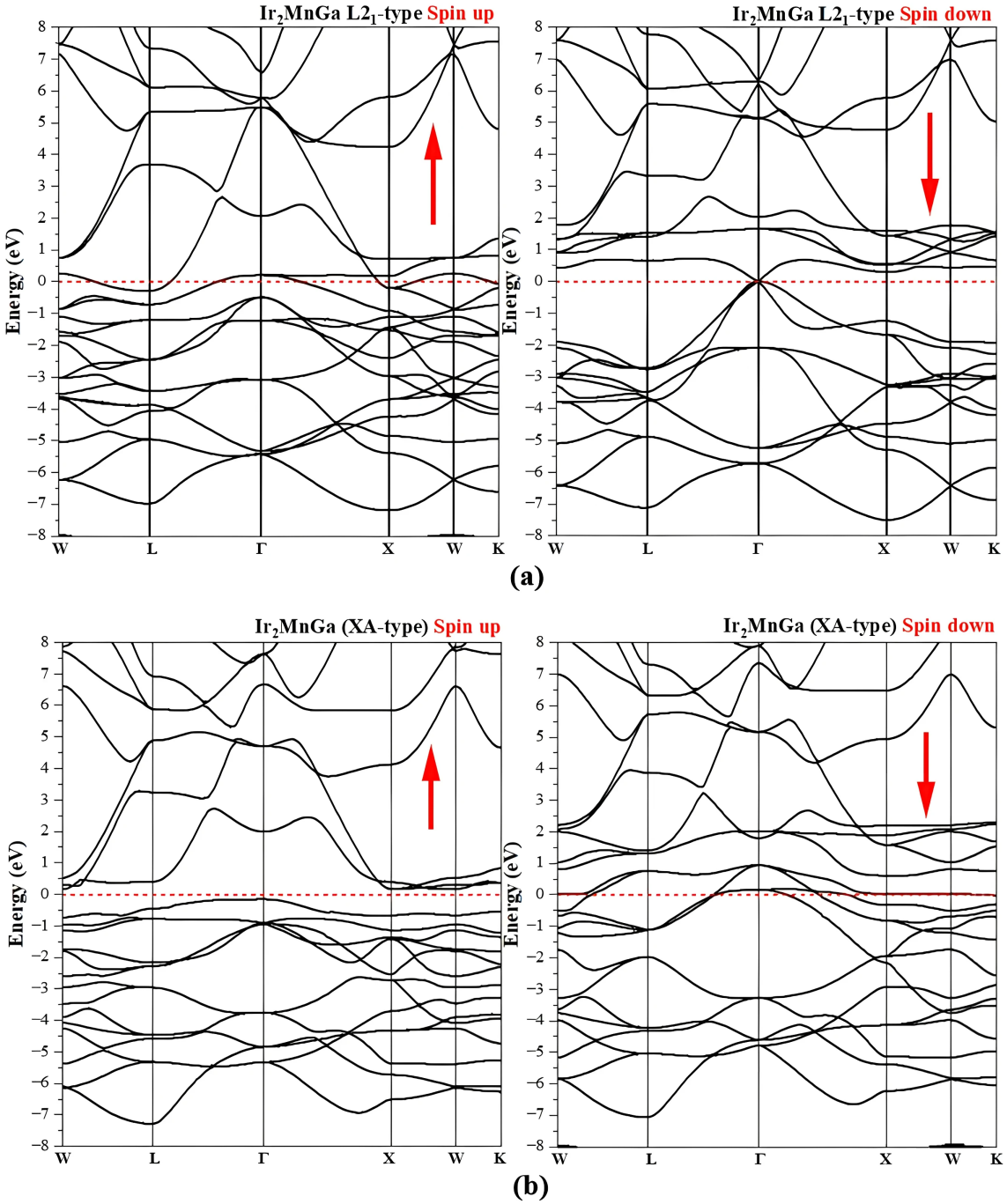

Figure 5. (Colour online) Spin-polarized band structure of Ir_2MnGa calculated using PBE+U (U = 4 eV) for both (a) $L2_1$-type and (b) XA-type structures.

For Ti_2MnGa, while the Ti contributions are more prominent in the conduction band (0 to 5 eV), there is a noticeable overlap with Mn in the upper valence band (−5 to 0 eV), suggesting a degree of covalent bonding due to hybridization between Ti and Mn atoms. This hybridization is particularly strong in the $L2_1$-type structure, where the symmetric arrangement of atoms maximizes orbital overlap. The Ga contributions, while less dominant, play a crucial role in mediating charge transfer between transition metal sites (Ti and Mn), particularly in the lower valence region (−8 to −7 eV).

For Ir_2MnGa, the Ir contributions are mainly concentrated around the Fermi level in the $L2_1$-type structure, showing strong overlap with Mn states in the range (−4 to 2 eV). This indicates significant hybridization, which promotes metallic behavior through enhanced electron delocalization. In contrast, the XA-type structure exhibits more localized Mn states near the Fermi level and weaker Ir contributions, reflecting reduced hybridization due to the lower symmetry. These differences highlight the sensitivity of the electronic structure to the atomic arrangement and symmetry.

The superior stability and metallic character of the $L2_1$-type structure arise from its enhanced hybridization and symmetric coordination, which promote electron delocalization, as observed in Ti_2MnGa. In contrast, the XA-type structure exhibits anisotropic hybridization, leading to more localized states and diverse electronic behavior, such as the half-metallic properties observed in Ir_2MnGa, including the possible formation of a gap in certain spin channels. These differences highlight the significant influence of crystal symmetry and atomic arrangement on the electronic properties of Heusler alloys, as confirmed by our calculations.

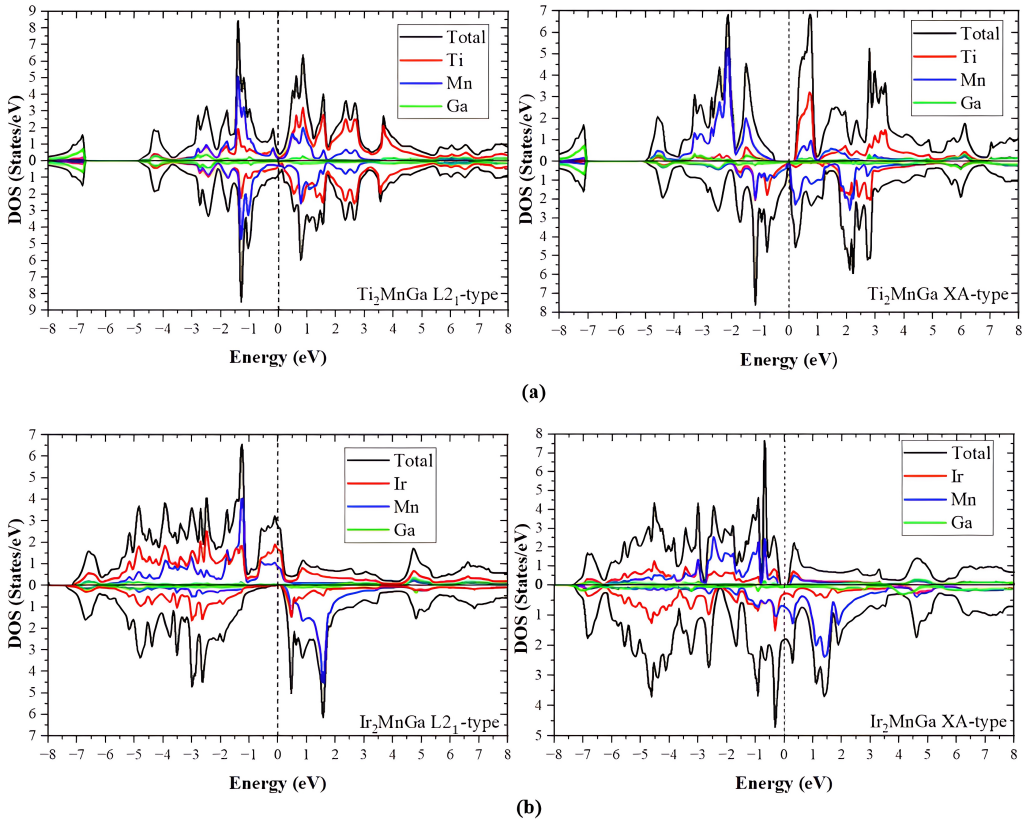

Figure 6. (Colour online) Spin-dependent total density of states for (a) Ti_2MnGa and (b) Ir_2MnGa calculated using PBE+U (U = 4 eV) in both $L2_1$-type and XA-type structures.

4.3. Magnetic properties

The magnetic moments of X_2MnGa (X = Ti, Ir) in $L2_1$ and XA structures were calculated via PBE+U (U = 4 eV). Table 2 shows the atom-resolved and total moments, revealing the impact of atomic species

and crystal symmetry. Comparison with the Slater–Pauling rule [41, 42] highlights deviations due to electronic localization and hybridization effects.

Table 2. Magnetic moments (in μ_B) of Ti_2MnGa and Ir_2MnGa compounds calculated via PBE+U.

Property	**$L2_1$ ($Fm\bar{3}m$)**		**XA ($F\bar{4}3m$)**	
	Ti_2MnGa	**Ir_2MnGa**	**Ti_2MnGa**	**Ir_2MnGa**
Interstitial moment M_{int}	−0.30669	0.08026	−0.75716	0.04452
Transition metal moment M_X (X = Ti/Ir)	−0.23601	0.12941	−0.28886	−0.24595
Manganese moment M_{Mn}	3.34682	3.39502	3.15768	3.44853
Gallium moment M_{Ga}	−0.02189	0.00140	−0.00306	−0.02329
Total magnetic moment M_{tot}	3.49026	3.99432	1.81973	2.97786

As shown in table 2, Mn exhibits the largest magnetic moment (3.16–3.45μ_B), considerably reduced from the expected 5μ_B for isolated Mn^{2+}. This reduction stems from three factors: strong Mn-3*d*/X-*d*/Ga-*p* hybridization, *d*-electron delocalization and crystal field effects.

Our calculated moments agree well with literature values: 3.99μ_B for Ir_2MnGa compared to the reported 4.02μ_B [43] and 3.49μ_B for Ti_2MnGa relative to 3.38μ_B [44], with minor differences attributable to computational parameters. The magnetic configuration shows antiferromagnetic Ti-Mn coupling (reducing the net moment) and structure-dependent Ir-Mn alignment.

Moment magnitudes vary with structure: the $L2_1$ phase shows higher moments (3.5–4.0μ_B) due to parallel alignment, while the XA phase exhibits reduced moments (1.8–3.0μ_B) from enhanced antiferromagnetic coupling. These results demonstrate the combined influence of spin alignment, local symmetry and electronic hybridization, validating our computational approach while revealing the parameter sensitivity.

5. Conclusion

This study reveals the fundamental structure-property relationships in Ti_2MnGa and Ir_2MnGa Heusler alloys through first-principles calculations. Three key findings emerge, the electronic ground state is highly sensitive to both composition and crystal symmetry, with Ti_2MnGa transitioning from spin gapless semiconductor (SGS) behavior in the XA-type structure (zero spin-↑ gap and 0.5 eV spin-↓ gap) to conventional ferromagnetic metallicity in the $L2_1$-type phase, while Ir_2MnGa shifts from gapless half-metallicity ($L2_1$) to conventional half-metallicity (XA-type). Magnetic properties are dominated by Mn-3*d* states with moments reduced to 3.16–3.45μ_B from the atomic 5μ_B limit due to strong *d*–*d*/*d*–*p* hybridization and crystal field effects. The Slater–Pauling rule partially governs the total moments, with deviations revealing complex interatomic exchange mechanisms. These results demonstrate how targeted substitutions (Ti, Ir) and structural control ($L2_1$, XA) can tune these alloys for specific spintronic applications requiring either fully spin-polarized transport (Ir-rich compositions) or low-power excitations (Ti-based SGS states).

Acknowledgements

The authors would like to express their sincere gratitude to the directors and staff of the respective research laboratories for their continuous support and for providing the necessary computational facilities and resources that made this work possible.

References

1. Palmstrøm C. J., Prog. Cryst. Growth Charact. Mater., 2016, **62**, 371–397, doi:10.1016/j.pcrysgrow.2016.04.020.
2. Chatterjee S., Chatterjee S., Giri S., Majumdar S., J. Phys.: Condens. Matter, 2022, **34**, 013001, doi:10.1088/1361-648X/ac268c.
3. Graf T., Felser C., Parkin S. S. P., In: Handbook of Spintronics, Xu Y., Awschalom D., Nitta J. (Eds.), Springer, Dordrecht, 2016, 335–364, doi:10.1007/978-94-007-6892-5_17.
4. Elphick K., Frost W., Samiepour M., Kubota T., Takanashi K., Sukegawa H., Mitani S., Hirohata A., Sci. Technol. Adv. Mater., 2021, **22**, 235–271, doi:10.1080/14686996.2020.1812364.
5. Hirohata A., Lloyd D. C., MRS Bull., 2022, **47**, 593–599, doi:10.1557/s43577-022-00350-1.
6. Galanakis I., In: Heusler Alloys, Vol. 222, Felser C., Hirohata A. (Eds.), Springer, Cham, 2016, 3–36, doi:10.1007/978-3-319-21449-8_1.
7. Gao G., Yao K., Appl. Phys. Lett., 2013, **103**, 232409, doi:10.1063/1.4840318.
8. Galanakis I., Özdoğan K., Aktaş B., Şaşioğlu E., Appl. Phys. Lett., 2006, **89**, 042502, doi:10.1063/1.2235913.
9. Skaftouros S., Özdoğan K., Şaşioğlu E., Galanakis I., Appl. Phys. Lett., 2013, **102**, 022402, doi:10.1063/1.4775599.
10. Wang X., Cheng Z., Wang J., Wang X., Liu G., J. Mater. Chem. C, 2016, **4**, 7176–7192, doi:10.1039/C6TC01343K.
11. Zhang Y. J., Liu Z. H., Liu E. K., Liu G. D., Ma X. Q., Wu G. H., Europhys. Lett., 2015, **111**, 37009, doi:10.1209/0295-5075/111/37009.
12. Amrich O., Monir M. E. A., Baltach H., Omran S., Sun X., Wang X., Al-Douri Y., Bouhemadou A., Khenata R., J. Supercond. Novel Magn., 2018, **31**, 241–250, doi:10.1007/s10948-017-4206-2.
13. Ahmed S., Zafar M., Rizwan M., Khan M. I., Arshad H., Jin H., Shabbir M., Al-Sehemi A. G., Shakil M., Indian J. Phys., 2021, **95**, 841–849, doi:10.1007/s12648-020-01739-x.
14. Şaşioğlu E., Sandratskii L. M., Bruno P., Phys. Rev. B, 2008, **77**, 064417, doi:10.1103/PhysRevB.77.064417.
15. Aguayo A., Murrieta G., J. Magn. Magn. Mater., 2011, **323**, 3013–3017, doi:10.1016/j.jmmm.2011.06.038.
16. Semiannikova A. A., Perevozchikova Yu. A., Irkhin V. Yu., Marchenkova E. B, Korenistov P. S., Marchenkov V. V., AIP Adv., 2021, **11**, 015139, doi:10.1063/9.0000118.
17. Marchenkov V. V., Kourov N. I., Belozerova K. A., Emelyanova S. M., Dyakina V. P., Marchenkova E. B., Eisterer M., Weber H. W., J. Phys.: Conf. Ser., 2014, **568**, 052019, doi:10.1088/1742-6596/568/5/052019.
18. Chen Z., Liu W., Chen P., Ruan X., Sun J., Liu R., Gao C., Du J., Liu B., Meng H., Zhang R., Xu Y., Appl. Phys. Lett., 2020, **117**, 012401, doi:10.1063/5.0013656.
19. Stinshoff R., Nayak A. K., Fecher G. H., Balke B., Ouardi S., Skourski Y., Nakamura T., Felser C., Phys. Rev. B, 2017, **95**, 060410, doi:10.1103/PhysRevB.95.060410.
20. Gavrea R., Hirian R., Isnard O., Pop V., Benea D., Solid State Commun., 2020, **309**, 113812, doi:10.1016/j.ssc.2020.113812.
21. Khan M., Jung J., Stoyko S. S., Mar A., Quetz A., Samanta T., Dubenko I., Ali N., Stadler S., Chow K. H., Appl. Phys. Lett., 2012, **100**, 172403, doi:10.1063/1.4705422.
22. Zheng H., Wang W., Wu D., Xue S., Zhai Q., Frenzel J., Luo Z., Intermetallics, 2013, **36**, 90–95, doi:10.1016/j.intermet.2013.01.012.
23. Nambiar S. S., Murthy B. R. N., Sathyashankara S., Prasanna A. A., J. Phys.: Conf. Ser., 2021, **2070**, 012231, doi:10.1088/1742-6596/2070/1/012231.
24. Chen X., Huang Y., Yuan H., Liu J., Chen H., Appl. Phys. A, 2018, **124**, 2259, doi:10.1007/s00339-018-2259-0.
25. Lukashev P., Kharel P., Gilbert S., Staten B., Hurley N., Fuglsby R., Huh Y., Valloppilly S., Zhang W., Yang K., Skomski R., Sellmyer D. J., Appl. Phys. Lett., 2016, **108**, 141901, doi:10.1063/1.4945600.
26. Fan L., Chen F., Li C., Hou X., Zhu X., Luo J., Chen Z., J. Magn. Magn. Mater., 2020, **497**, 166060, doi:10.1016/j.jmmm.2019.166060.
27. Blaha P., Schwarz K., Sorantin P., Trickey S. B., Comput. Phys. Commun., 1990, **59**, 399–415, doi:10.1016/0010-4655(90)90187-6.
28. Tran F., Blaha P., Schwarz K., Novák P., Phys. Rev. B, 2006, **74**, 155108, doi:10.1103/PhysRevB.74.155108.
29. Argaman N., Makov G., Am. J. Phys., 2000, **68**, 69–79, doi:10.1119/1.19375.
30. Perdew J. P., Burke K., Ernzerhof M., Phys. Rev. Lett., 1996, **77**, 3865–3868, doi:10.1103/PhysRevLett.77.3865.
31. Taş M., Şaşioğlu E., Blügel S., Mertig I., Galanakis I., Phys. Rev. Mater., 2022, **6**, 114401, doi:10.1103/PhysRevMaterials.6.114401.
32. Wang X., Li T., Cheng Z., Wang X., Chen H., Appl. Phys. Rev., 2018, **5**, 041103, doi:10.1063/1.5042604.
33. Wang X., Cheng Z., Zhang G., Yuan H., Chen H., Wang X., Phys. Rep., 2020, **888**, 1–57, doi:10.1016/j.physrep.2020.08.004.
34. Liu Z., Liu J., Zhao J., Nano Res., 2017, **10**, 1972–1979, doi:10.1007/s12274-016-1384-3.

35. Belashchenko K. D., Glasbrenner J. K., Wysocki A. L., Phys. Rev. B, 2012, **86**, 224402, doi:10.1103/PhysRevB.86.224402.
36. Shaughnessy M., Snow R., Damewood L., Fong C. Y., J. Nanomater., 2011, **2011**, 140805, doi:10.1155/2011/140805.
37. Jedema F. J., Nijboer M. S., Filip A. T., van Wees B. J., Phys. Rev. B, 2002, **67**, 085319, doi:10.1103/PhysRevB.67.085319.
38. Murnaghan F. D., Proc. Natl. Acad. Sci. U. S. A., 1944, **30**, 244–247, doi:10.1073/pnas.30.9.244.
39. Goraus J., Czerniewski J., Balin K., Fijałkowski M., Prusik K., Chrobak A., Mater. Charact., 2019, **154**, 248–252, doi:10.1016/j.matchar.2019.06.007.
40. Balakrishnan K., Alagarsamy S., Veerapandy V., Phys. Status Solidi B, 2022, **260**, 2200329, doi:10.1002/pssb.202200329.
41. Slater J. C., Phys. Rev., 1936, **49**, 931–937, doi:10.1103/PhysRev.49.931.
42. Pauling L., Phys. Rev., 1938, **54**, 899–904, doi:10.1103/PhysRev.54.899.
43. Krishnaveni S., Mater. Res. Express, 2019, **6**, 096545, doi:10.1088/2053-1591/ab2ec4.
44. Jia H. Y., Dai X. F., Wang L. Y., Liu R., Wang X. T., Li P. P., Cui Y. T., Liu G. D., AIP Adv., 2014, **4**, 047113, doi:10.1063/1.4871403.

Поза межами звичайних напівметалів: безщілинні стани та безщілинна спінова напівпровідникова поведінка в сполуках Гейслера X_2MnGa (X = Ti, Ir)

Н. Бутельджа[1], Н. Хачіні[2], І. Уадха[3], Х. Рашед[3]

[1] Лабораторія теоретичної фізики та фізики матеріалів, Університет Хассіба Бенбуалі, Шлеф, Алжир

[2] Лабораторія конденсованих систем, Оран 1 Університет Ахмеда Бен Белли, Оран, Алжир

[3] Лабораторія магнітних матеріалів, Університет Джиллалі Ліабес, Сіді-Бель-Аббес, Алжир

Пошук високопродуктивних спінтронних матеріалів мотивує дослідження сплавів Гейслера з нетрадиційними електронними властивостями. Використовуючи теорію функціоналу густини з поправкою Хаббарда (DFT+U, $U = 4$ eV), ми досліджуємо сплави X_2MnGa (X = Ti, Ir), які стабілізуються у феромагнітній структурі типу $L2_1$ з сильною термодинамічною стійкістю. Розрахунки виявляють різну поведінку електронної структури: Ti_2MnGa переходить з металевої фази типу $L2_1$ у спін-безщілинний напівпровідник (SGS) типу XA, тоді як Ir_2MnGa демонструє безщілинну напівметалеву поведінку у типі $L2_1$, але стає напівметалевим у типі XA. Магнітні властивості визначаються *spd* гібридизацією між станами Mn-3d та X-d/Ga-p, яка стабілізує феромагнетизм та адаптує електронні стани поблизу рівня Фермі. Поправка Хаббарда U виявляється важливою для точного опису скорельованих електронів Mn-3d. Ці сплави поєднують структурну стабільність з регульованими електронними та магнітними властивостями, створюючи перспективну основу для спін-поляризованого переносу в спінтроннічних пристроях наступного покоління.

Ключові слова: *сплави Гейслера, спінтроніка, DFT+U, спінові безщілинні напівпровідники, напівметали, магнітні матеріали*